Croatian Society for Materials Protection

Metalurgija/Metallurgy

Vol. 65 No. 3 / 2026

Printed PZT Sensors and Machine Learning for Intelligent Fault Diagnosis in EMS Trays

Xiaolong Wu [1], Dongjiong Xu [1], Anjie Zheng [1], Min Xu [1], Leilei Zhu [1,*], Bin Lin [1], Chao Zheng [1], Kelei Sun [1], Yexin Wang [2,3], and Kai Li [2,3,*]

https://doi.org/10.64486/m.65.3.8

[1] Ningbo Cigarette Factory, Zhejiang China Tobacco Industry Co., LTD., 2001 Jiapu West Road, Fenghua Economic Development Zone, Ningbo 315040, China
[2] Key Laboratory of Impact and Safety Engineering, Ministry of Education, Ningbo University, No.818 Fenghua Road, Jiangbei District, Ningbo, Zhejiang, 315211, China
[3] School of Mechanical Engineering and Mechanics, Ningbo University, No.818 Fenghua Road, Jiangbei District, Ningbo, Zhejiang, 315211, China
* Correspondence: 459529249@qq.com; likai@nbu.edu.cn

Type of the Paper: Article
Received: July 15, 2025
Accepted: December 28, 2025

Abstract: Fault diagnosis in highly automated and sealed EMS trays presents significant challenges. This study proposes a novel method utilizing printed lead zirconate titanate (PZT) strain sensors combined with machine learning. Micro/nanoscale PZT structures were fabricated via printing, and the impact of annealing on their crystallization, microstructure, and resultant piezoelectric/dielectric properties and impedance characteristics (for both thick films and 3D structures) was investigated. A neural network model was developed, with its hyperparameters (weights, thresholds, and topology) optimized using a Bayesian approach. Comparative analysis of model performance demonstrated the method's effectiveness in achieving accurate fault diagnosis for EMS electric vehicle systems, providing valuable theoretical and technical support for their detection, operation, and maintenance.

Keywords: 3D printing; PZT; EMS trolley; fault diagnosis; machine learning

1. Introduction

The Electric Monorail System (EMS) trolley system was widely used in the logistics transportation of tobacco shreds in the elevated warehouse [1, 2]. However, its high automation, enclosed design, and large fleet size make real-time operational monitoring and fault diagnosis exceptionally challenging. Traditional manual inspection and simple data analysis methods fail to meet the demand for high-precision, adaptive anomaly detection in such complex systems.

Although traditional strain sensors have been maturely applied in the field of industrial inspection, their inherent limitations become prominent when dealing with the special shape requirements of EMS trolley tracks [3, 4]. Standardized rectangular or grid structures cannot fit complex curved surfaces, and forced installation may lead to stress concentration or measurement distortion [5]. Traditional photolithography processes require steps such as masks and etching, which lead to a sharp increase in the cost of small-batch customization and a design iteration cycle that lasts for several weeks [6]. The three-dimensional (3D) printing path can be directly programmed and controlled based on the computer-aided design (CAD) model, and any topological structure (fractal curve, bionic web, etc.) can be generated [7-9]. Many breakthroughs have made printing technology a core enabling tool in cutting-edge fields such as large-scale infrastructure monitoring [10-12]. Among various

3D printing technologies, electrohydrodynamic 3D printing has the advantages of low cost, high efficiency, and strong controllability. By using a uniformly dispersed nanoscale suspension, the electrohydrodynamic 3D printing could produce target structures with good uniformity, consistency, and density [13, 14]. Moreover, it had good compatibility with suspension materials and substrate materials, and was widely applied in fields such as biology, energy, and food [15]. Using electrohydrodynamic 3D printing to fabricate customized high-performance sensors was a powerful approach [16, 17].

In recent years, deep learning methods represented by neural network algorithms have shown significant advantages in the fields of time series data analysis, pattern recognition, and prediction, providing an effective technical path for the fault diagnosis of EMS trolley systems [18-20]. Li proposed a lightweight convolutional neural network (CNN) based on MobileNetV2 to classify fresh tobacco leaves into 12 maturity types, achieving high accuracy with fewer parameters and computations [21]. It showed that neural networks could deeply analyze massive data to uncover internal relationships and key features, adapt efficiently to high-dimensional data models, and enable intelligent data processing and decision-making. However, there was currently no neural network model specifically designed for the operational status and fault detection of EMS trolley systems. Therefore, there was an urgent need to design and construct prediction models to ensure the accuracy of operational status identification.

To enhance the fault diagnosis capability of the EMS trolley system, this study proposes an innovative solution by deeply integrating customizable printed PZT strain sensor technology with a neural network hyperparameter automatic optimization method based on Bayesian optimization, constructing a complete framework from physical sensing to intelligent diagnosis. Specifically, the research first utilizes electrospray deposition technology to prepare PZT sensors suitable for complex track surface geometries. Through systematic investigation of the effects of annealing processes on their crystal phase, microstructure, and final piezoelectric/dielectric properties, the optimal fabrication parameters for the sensors were determined. Building on this, strain signals during trolley operation were collected via a self-developed signal detection system and processed using methods such as wavelet packet transform for denoising and feature extraction. Regarding the diagnostic model, instead of directly applying existing networks, this study introduces a Bayesian optimization framework that automatically searches and determines the key structural and training hyperparameters of the neural network (such as the number of neurons, regularization strength, activation function, etc.) tailored for the multi-condition classification task of EMS trolleys, thereby constructing a customized optimal diagnostic model. Test results show that the diagnostic accuracy of this optimized model reaches as high as 91.07 %. To further validate the superiority of the proposed framework, a Hybrid Genetic Particle Swarm Optimization (HGAPSO)-optimized neural network model was also constructed for comparative analysis, achieving a diagnostic accuracy of 86.5 %, which represents an average improvement of 8.16 % compared to models optimized solely by Genetic Algorithm or Particle Swarm Optimization. This study successfully achieves precise identification of the operating status of EMS trolleys, providing integrated theoretical and technical support-from novel sensing hardware to dedicated diagnostic algorithms-for addressing the challenges of real-time condition monitoring and intelligent maintenance of equipment in highly automated, enclosed logistics systems.

2. Materials and Methods

2.1 3D printing experimental platform

The PZT structure printing experimental platform consists of a micro-injection pump (PHD ULTRA 70-3307, Harvard Instruments, USA), a DC high-voltage power supply (DWP-P502-50ACF3, Dongwen High Voltage Power Supply Co., Ltd., Tianjin, China), an X-Y axis motion platform, a Z-axis motion platform, a microscope camera (SJM-500Y, Visual Me Co., Ltd., Taiwan, China), a spray needle and a computer.

2.2 PZT slurry

The PZT powder (PZT-5H, Baoding Hongsheng Acoustic Electronic Equipment Co., Ltd., China Hebei) and PZT sol were preliminarily mixed. Then, the suspension after the preliminary mixing was subjected to ball

https://doi.org/10.64486/m.65.3.8

milling using a planetary ball mill (QM-3SP2, Nanjing Nan Da Instrument Factory, China Jiangsu). The ball milling process parameters were set as follows: the angular velocity of the outer cylinder was 19.9 rad s^{-1}, the angular velocity of the inner cylinder was 39.8 rad s^{-1}, and the ball milling time was 50 hours.

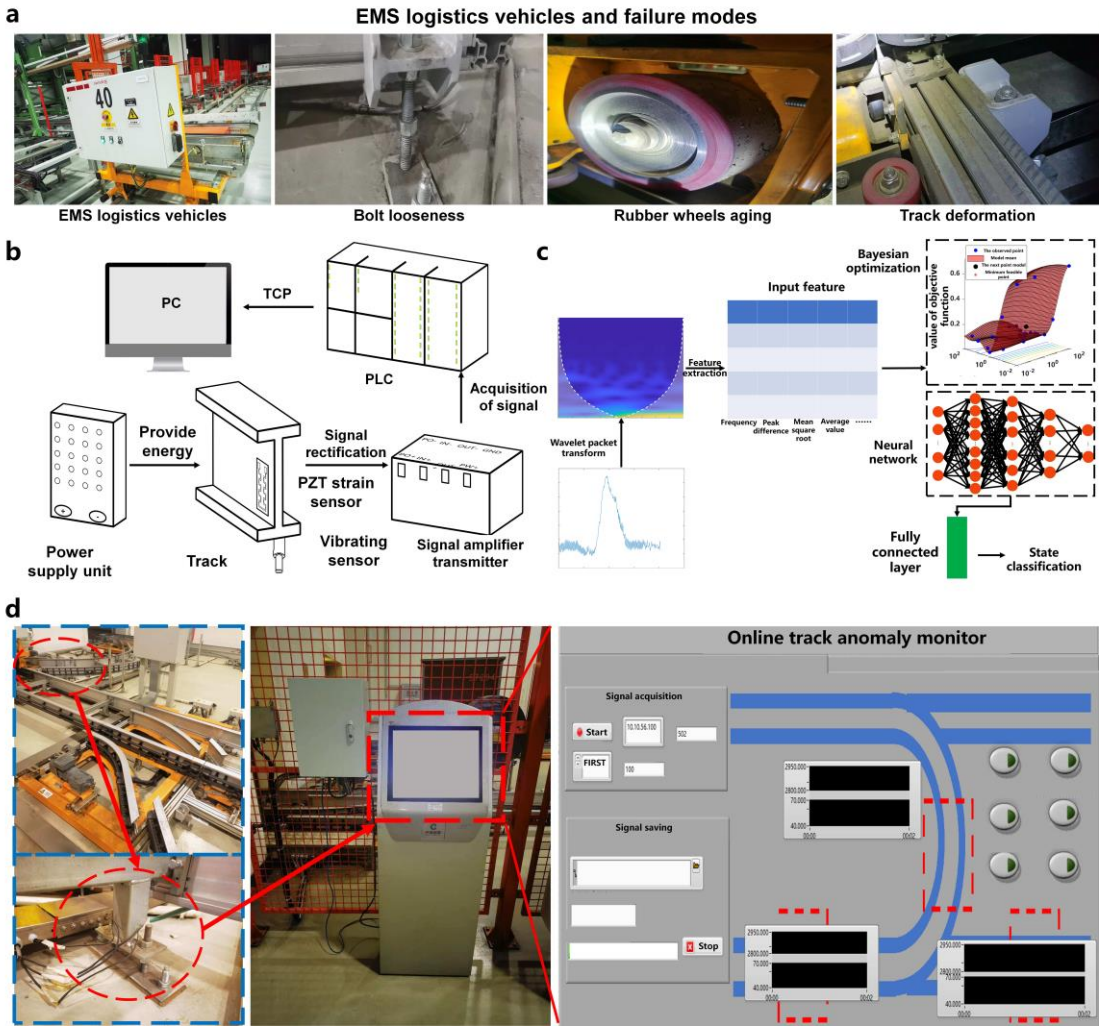

Figure 1. EMS Trolley Track Strain Monitoring System. (a) EMS logistics vehicles and failure modes, (b) Schematic diagram of the signal detection scheme, (c) Overall framework of the deep learning model, (d) Online monitoring interface.

2.3 Signal detection system

The self-developed EMS trolley system signal detection system was composed of an upper computer, PLC configuration hardware (including central processing unit module, analog signal input module, Ethernet communication module), signal amplification transmitter, PZT strain gauge, and power supply. Among them, the central processing unit module (CPU311-1), the analog signal input module (AI308-1), and the Ethernet communication module (CM304-1) were purchased from Zhejiang Zhongkong Research Institute Co., LTD., and the signal amplification transmitter (IBF15-Po2-2mV/V-P1-A4) was purchased from Beifu Technology Co., LTD. The strain gauge was printed and prepared in the laboratory. The power supply (S-75-24) was purchased from genuine Mean Well Co., LTD. This system conducts operation status identification by real-time monitoring of the strain signals generated during the operation of the EMS trolley on the track, combined with the data processing device and the visual monitoring interface. Strain sensors were arranged at key positions on the track to collect the strain signals caused by the operation of the trolley. The PLC configuration module was responsible for receiving the raw signals collected by the sensors and transmitting them to the upper computer for

https://doi.org/10.64486/m.65.3.8

signal filtering, feature extraction and state assessment, and ultimately generating intuitive visualization results, as shown in Figure 1. Figure 1a provides the application context and defines the core problem. It depicts a standard EMS trolley system within the elevated warehouse logistics network and outlines the primary failure modes targeted for diagnosis in this study. These include motor drive anomalies, guide wheel wear or jamming, and structural imbalances during loading/unloading operations, all of which manifest as unique signatures in the track strain signals. The practical implementation of the signal detection scheme is shown in Figure 1b. It details the on-site installation of the printed PZT strain gauge on the trolley rail, the wiring to the signal conditioning module, and the data transmission path to the PLC and upper computer. Figure 1c presents the overall framework of the proposed deep learning-based fault diagnosis model. The framework begins with the acquisition of raw strain signals from the sensors. These signals first undergo preprocessing, including wavelet packet-based denoising and time-frequency transformation for feature extraction. The processed feature set is then fed into a neural network, the hyperparameters of which (e.g., layer size, learning rate) are automatically optimized using a Bayesian optimization algorithm to achieve optimal performance. Finally, the optimized model performs state classification, identifying the specific operating or fault condition of the trolley. The PLC configuration transmits the original signal to the monitoring system to achieve real-time monitoring of the strain signal. Ultimately, the system presents the signal monitoring results in a graphical interface, facilitating users to intuitively grasp the operating status of the trolley, as shown in Figure 1d.

2.4 Data preprocessing

In this paper, the self-developed EMS trolley system signal detection system was adopted to collect the track strain signal of the EMS trolley. The communication address of the collected signal was set as 10.10.56.100, and the reading port was 502. According to the address of the PLC and the communication protocol, the reading address sequence number was converted to 16. During each test process, 100,000 test collection points were set up, with a collection frequency of 200 Hz, to collect the strain signals of different EMS trolleys passing through specific tracks. To eliminate the high-frequency noise interference in the collected signal of the EMS trolley strain sensor, the wavelet packet transform was adopted to perform multi-scale decomposition and noise reduction processing on the original signal. Wavelet Packet Transform (WPT) was an extension of Wavelet transform, allowing for more flexible decomposition of the high-frequency and low-frequency parts of the signal. Its core formulas include the recursive definition, decomposition, and reconstruction algorithms of wavelet packet functions. The wavelet packet function as shown in equation (1)

$$\begin{aligned} W_{2n}(t) &= \sqrt{2}\sum_k h_k \cdot W_n(2t-k) \\ W_{2n+1}(t) &= \sqrt{2}\sum_k g_k \cdot W_n(2\,\mathrm{t}-\mathrm{k}) \end{aligned} \tag{1}$$

where n is the wavelet packet node index, with initial conditions $W_0=\phi(t)$, $W_1=\psi(t)$. h_k and g_k represent the low-pass and high-pass filter coefficients, respectively. Wavelet packet decomposition refers to the process in which the coefficients $w_{j,n}[k]$ of a signal x(t) at node j in the k decomposition level can be recursively decomposed into two child nodes at the next level. This is expressed by equation (2) as

$$\begin{aligned} W_{j+1,2n}[m] &= \sum_k h[k-2m]\times W_{j,n}[k] \\ W_{j+1,2n+1}[m] &= \sum_k g[k-2m]\times W_{j,n}[k] \end{aligned} \tag{2}$$

where h and g are the decomposition filters, and m is the index of the child node coefficients. The reconstruction algorithm primarily restores the parent node coefficients from the child node coefficients, as shown in equation (3):

$$w_{j,n}[k] = \sum_m h[k-2m]\cdot w_{j+1,2n+1}[m] + \sum_m g[k-2m]\cdot w_{j+1,2n+1}[m] \tag{3}$$

https://doi.org/10.64486/m.65.3.8

where h and g are the reconstruction filters. The signal obtained by wavelet packet transformation is denoised, with the corresponding denoising formula given in equation (4)

$$w_{j,k} = x_{j,k} + y_{j,k} \tag{4}$$

where $x_{j,k}$ generally denotes the wavelet coefficients corresponding to non-noise or useful signals, and $y_{j,k}$ represents the wavelet coefficients typically associated with noise or other interference signals. The wavelet packet time-frequency transform utilizes the time-frequency localization properties of wavelet packet basis functions to perform time-frequency conversion. The core equations include the time-frequency parameters of the wavelet packet basis functions and the mathematical expressions of time-frequency energy distribution. For the time-frequency parameters of wavelet packet basis functions, each basis function corresponds to a time-frequency window, with its center time and center frequency calculated using the formulas given in equation (5)

$$\begin{aligned} t_{j,n} &= \frac{\int t\,|W_{j,n}(t)|^2\,dt}{\int |W_{j,n}(t)|^2\,dt} \\ \omega_{j,n} &= \frac{\int \omega\,|W_{j,n}(\omega)|^2\,d\omega}{\int |W_{j,n}(\omega)|^2\,d\omega} \end{aligned} \tag{5}$$

where j is the decomposition level, n is the node index, and $W_{j,n}(\omega)$ is the Fourier transform of the wavelet packet basis function $W_{j,n}(t)$. The width of the time-frequency window is determined by the time-domain and frequency-domain variances of the basis function. The time-frequency transformation of a signal can be expressed as Equation (6)

$$E(j,n,m) = \left|\omega_{j,n}[m]\right|^2 \tag{6}$$

where m is the time index, corresponding to the time position of the signal $t = m \times 2\text{-}j$. The index n determines the frequency band range, with the center frequency given by $\omega_{j,n}$. This paper primarily adopts the Continuous Wavelet Packet Transform (CWPT). After wavelet packet decomposition and denoising, the signal is subjected to time-frequency transformation using the continuous wavelet packet transform function. The corresponding formula is given in equation (7)

$$TFR_x(t,\omega) = \sum_{j,n} \langle x, W_{j,n} \rangle \cdot W_{j,n}(t) \cdot \chi_{j,n}(\omega) \tag{7}$$

where $<x, W_{j,n}>$represents the wavelet packet coefficients, and $\chi_{j,n}(\omega)$ is the frequency band labeling function. Considering the differences in strain response characteristics of EMS trolleys under various operating conditions, a windowed sliding segmentation signal processing algorithm was applied to segment and label the continuous strain signals, as shown in Table 1.

Table 1. Classification information of the signals generated by the four EMS trolleys

Classification	The signal generated by the EMS trolley
1	EMS trolley without material box (empty state)
2	The EMS trolley with an empty box (loaded with an empty box status).
3	The EMS trolley with a material box(loaded with a full box status).
4	EMS trolley loading and unloading box (empty loading state)

https://doi.org/10.64486/m.65.3.8

2.5 Neural network

The neural network was a type of multilayer feedforward neural network that was widely used in fields such as classification and pattern recognition. This model employs a multilayer structure and optimizes model weights through the error backpropagation algorithm, significantly enhancing its capability to handle nonlinear problems and improving classification and pattern recognition performance. During each training iteration, input data first enters the network through the input layer and is propagated layer by layer to the output layer, where the network's prediction results are generated. Each neuron in a layer produces output based on the outputs and connection weights from the previous layer. Once the prediction results were produced, they were compared with the expected outputs to calculate the error. A commonly used error metric was the Mean Squared Error (MSE) [25-27], which was calculated as shown in Equation (8)

$$\mathrm{MSE} = \frac{1}{N}\sum_{i=1}^{N}(y_{\mathrm{pred}}^{(i)} - y_{\mathrm{true}}^{(i)})^2 \tag{8}$$

where $y_{pred}^{(i)}$ represents the predicted value, and $y_{true}^{(i)}$ represents the actual value. The backpropagation algorithm applies the chain rule to propagate the error from the output layer backward through the hidden layers, sequentially computing the gradients for each layer's weights, thereby enabling efficient optimization of the model parameters. Once the gradients were obtained, the model updates the weights and biases using the gradient descent method, gradually minimizing the error. Gradient descent [28-30] performs the update according to the following equation (9)

$$W = W - \eta \cdot \frac{\partial E}{\partial W} \tag{9}$$

where η is the learning rate, controls the step size of each update, E is the calculated value and W is the deviation value.

The training of neural networks usually stops under the following two circumstances: one was when the error reaches the preset threshold, and the other is when the maximum number of training rounds is reached. This process ensures that the network avoids overfitting while minimizing errors as much as possible. Take the 3-layer hidden layer as an example. The dimension of the initial input data was 11 dimensions, forming a 540 (11) dataset. The first layer was the hidden layer. For the first step of neural learning on the dataset, the number of neurons was 220, and the activation function was the hyperbolic tangent (Tanh) function. The Tanh function was chosen for its zero-centered output range [-1, 1], which promotes faster convergence during gradient-based optimization compared to non-zero-centered functions like Sigmoid. Its smooth non-linearity is effective for capturing the complex patterns present in the preprocessed strain signal data. The second hidden layer conducts bundle learning on the dataset of the first layer and passes it to the next layer according to the learning weights. The size of this hidden layer was 300 and the activation function was again Tanh, maintaining consistency in gradient flow through these intermediate layers. The third layer was the hidden layer. Neural learning was conducted based on the output data of the second layer. The output layer, based on the neural learning within the model, outputs the learning structure in the hidden layer to predict the classification results of the signals generated by different EMS carts.

2.6 Hyperparameter optimization

Hyperparameter optimization refers to the process parameters before training a prediction model to optimize its performance[31, 32]. Key hyperparameters that control the learning process include learning rate, hidden layer size, and regularization coefficients. Proper hyperparameter settings help to avoid underfitting and overfitting, thereby enhancing the model's generalization ability. Bayesian optimization was employed as the optimization method. The Bayesian optimization framework includes Gaussian process regression and an acquisition function[33-35]. Bayesian optimization uses a Gaussian process to model the posterior distribution of

https://doi.org/10.64486/m.65.3.8

the objective function, assuming that the objective function for hyperparameters follows a Gaussian process [36-38], as shown in equation (10)

$$f(\theta) = GP\left(\mu(\theta), k(\theta, \theta')\right) \tag{10}$$

where $\mu(\theta)$ is the mean function, and $k(\theta, \theta')$ is the covariance function used to define the correlation between input points. In the Gaussian process, a predictive function is used to perform regression on the data to conform to the Gaussian distribution. The predictive mean and variance are as shown in equation (11)

$$\mu_n(\theta) = \mathbf{k}_n^T \mathbf{K}_n^{-1} \mathbf{y}_n, \sigma_n^2(\theta) = k(\theta, \theta) - \mathbf{k}_n^T \mathbf{K}_n^{-1} \mathbf{k}_n \tag{11}$$

where K_n is the covariance matrix of the training data, k_n is the covariance vector between the new point and the training points, and y_n is the vector of observed values. The toolbox was primarily used to iteratively optimize the neural network hyperparameters, mainly employing the expected improvement function, as shown as equation (12).

$$EI(\theta) = \mathrm{E}[\max(0, f^* - f(\theta))] \tag{12}$$

2.7 Modeling

Figure 1c shows the overall framework of the model, which consists of two main parts: Bayesian hyperparameter optimization and a neural network. Firstly, the strain signals under different states were collected by sensors. The strain signals collected by the sensors were processed by using the time window and wavelet packet algorithm, and the strain signals were labeled. The processed signals were subjected to time-frequency transformation and time-domain data extraction to extract signal features. The Bayesian optimization proposed in this paper iterates over the hyperparameter data within the neural network to search for the optimal combination of hyperparameters. After multiple iterations, the internal hyperparameter optimization proposal was introduced into the neural network for training and learning to obtain the optimal network model. Finally, the status classification was completed through the fully connected layer, and the fault types were identified for different states. The learning and training models used in this paper all adopt the same parameter settings. The loss function uses the multi-class cross-entropy function. The number of generations selected was 50 times, and the input batch size was set to 15.

3. Results and discussion

3.1 Preparation and characterization of PZT sensors

The schematic diagram of electrohydrodynamic jet deposition for PZT thick film deposition is shown in Figure 2a. It was a material deposition technology based on electrohydrodynamics. The ink will be subjected to additional normal and tangential electric field forces. Under the action of the complex force, the liquid forms stable Taylor cones and nanoscale droplets. Supplemented by controllable deposition pathways, electrohydrodynamic jet deposition can be achieved on the basal pattern preparation of a variety of materials. The schematic diagram of the post-processing procedure for PZT The sintering annealing process of thick film was shown in figure 2b. PZT ceramic material was the densification and crystal phase transformation process of PZT under certain annealing temperature and annealing time conditions. An appropriate sintering annealing process was crucial for the transformation from non-perovskite structural components to perovskite structural components in PZT material.

The PZT thick films after annealing treatment at 720 °C and 820 °C obtain a complete perovskite structure (Figure 2c) without the generation of impurity phases. The PZT thick film, after annealing treatment at 920 °C has produced impurity phases. The impurity phase situation in the PZT thick film after annealing treatment at 1000 °C was more serious. After annealing at 1100 °C, the heterophase peaks of the PZT thick film have completely lost the perovskite peak positions. The surface morphology of PZT thick films with different annealing

https://doi.org/10.64486/m.65.3.8

treatments (figure 2d). The grain boundaries were smooth, and the surface roughness and flatness of the thick films gradually deteriorated with the increase of annealing temperature. The PZT thick film treated by annealing at 1000 °C shows obvious grain coarsening, the intergrain bonding deteriorates, the porosity increases, and the overall density of the thick film decreases. However, for the PZT thick film that was annealed at 1100 °C, the phenomenon of grain coarsening occurred. The surface of the thick film was uneven, and the roughness was extremely poor. From this, it can be known that 720 °C was a more suitable annealing temperature for PZT thick films. The PZT after annealing the structure elements was shown in figure 2e. The test results show that only by Pb, Zr, Ti, O four elements, showing that the PZT printing process after-treatment element does not appear in the process of annealing and erosion.

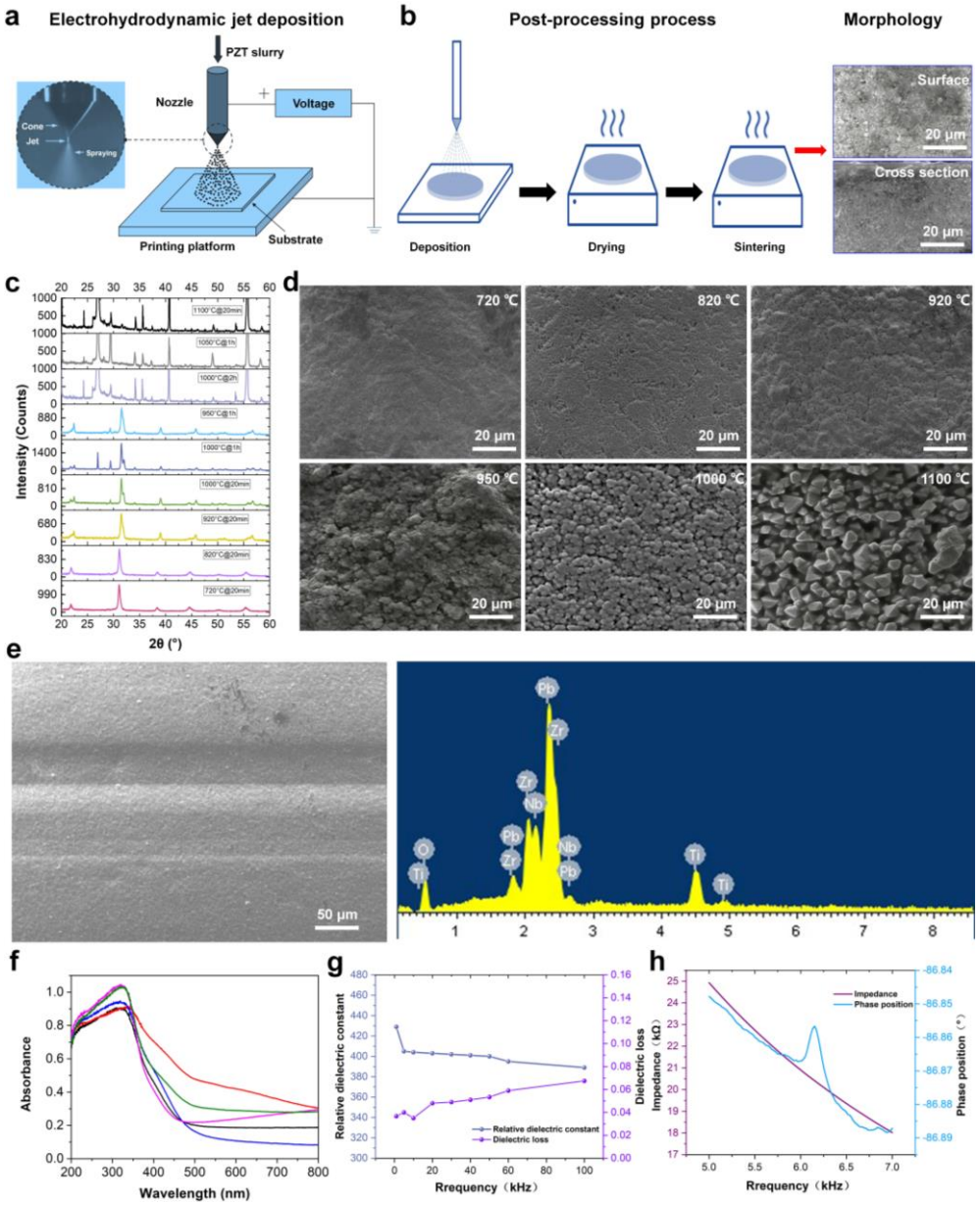

Figure 2. Preparation and characterization of PZT sensors. (a)Schematic diagram of electrohydrodynamic jet deposition for PZT thick film deposition, (b) Schematic diagram of the post-processing procedure for PZT thick film, (c) XRD patterns of PZT thick films annealed at different temperatures, (d) Surface SEM images of PZT thick films annealed at different temperatures, (e) PZT energy spectrum results, (f) Fourier transform infrared spectroscopy of sintered PZT, (g) Frequency dependence of relative permittivity and dielectric loss of PZT thick film, (h) Resonance frequency test curves.

https://doi.org/10.64486/m.65.3.8

The Fourier transform infrared spectroscopy of sintered PZT was shown in figure 2f. The results confirm that the main phase of perovskite exists, and there were no heterophases such as pyrogreen. The absorption rate spectra indicate that key chemical bonds such as Ti-O, Zr-O, and Pb-O exist well, which is consistent with the results of XRD and energy spectrum. The PZT sensor under 25 °C relative dielectric constant and dielectric loss with the change of test frequency (figure 2g). It can be seen from the figure that as the test frequency increases, the relative dielectric constant of the PZT sensor shows a downward trend, while the dielectric loss shows an upward trend. When the measurement frequency was 1 kHz, the relative dielectric constant and dielectric loss of the PZT sensor were 230 and 0.037, respectively. When the test frequency rises to 50 kHz, the relative dielectric constant of the PZT sensor drops to 198, and the dielectric loss rises to 0.053. When the test frequency rises to 100 kHz, the relative dielectric constant of the PZT thick film drops to 185, and the dielectric loss rises to 0.068.

The impedance characteristics of the 5-7 kHz of PZT sensor was shown in figure 2h. It can be known from the results that, compared with the piezoelectric sensor prepared by the traditional method of pasting piezoelectric sheets, the resonant frequency of the piezoelectric sensor prepared in this work has been significantly improved. This research work provides an efficient and simple preparation process for micro-deformation detection. Meanwhile, it has great potential to enhance the sensitivity of quality inspection.

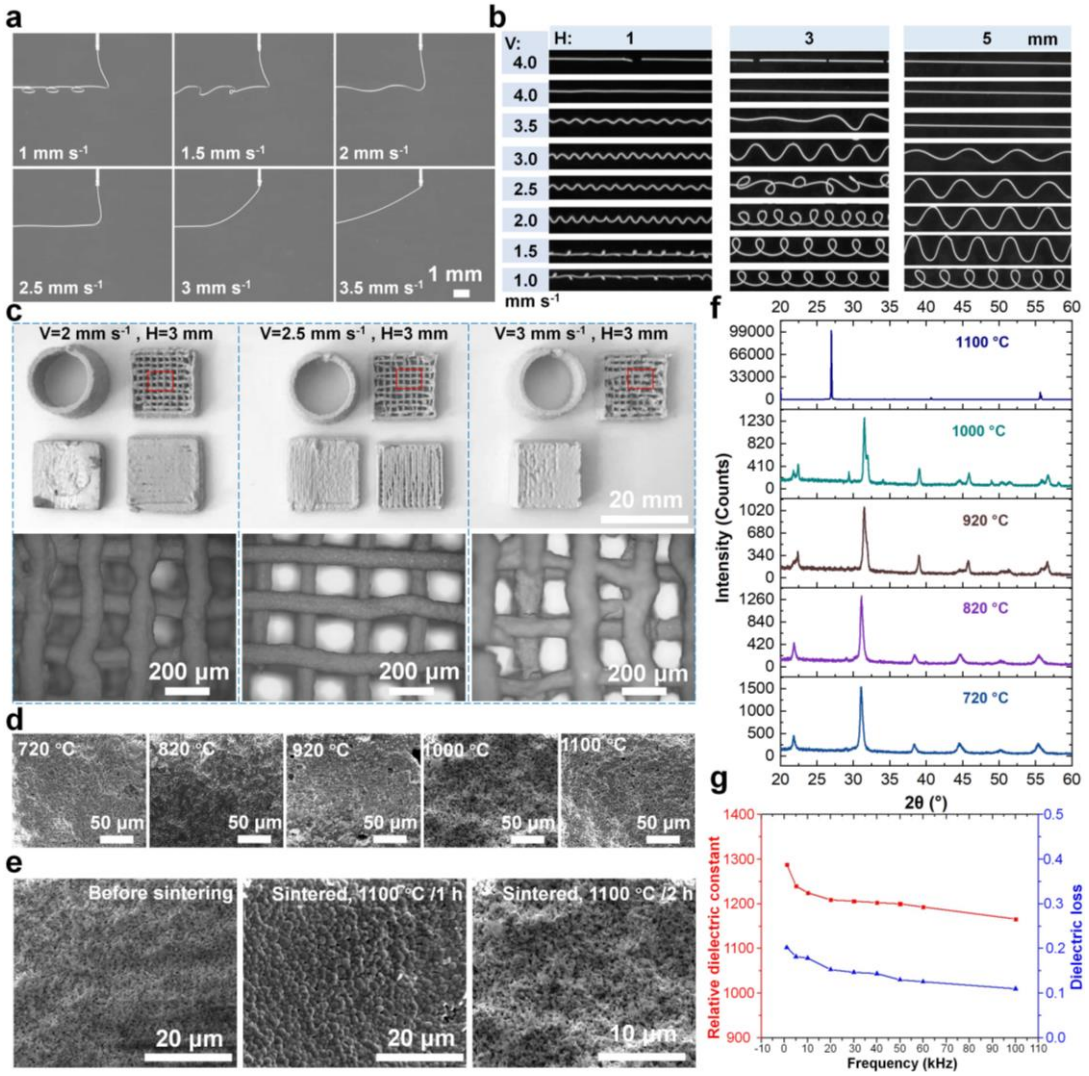

Figure 3. Preparation and characterization of PZT 3D structure. (a) Jet morphology under different printing speeds, (b) Structural morphology under different printing speeds and printing heights, (c) The printed 3D PZT structure under different printing conditions, (d) Surface SEM images of 3D structure annealed at different temperatures, (e) Surface SEM images

https://doi.org/10.64486/m.65.3.8

of 3D structure annealed at 1100 °C of different times, (f) XRD patterns annealed at different temperatures, (g) Frequency dependence of relative permittivity and dielectric loss of sintered PZT 3D structure.

The jet morphology under different printing speeds was shown in figure 3a. When the printing speed was 1 mm s^{-1}, uniform circular structures were printed; as the printing speed gradually increased, the radius of the circular structures gradually decreased, and then a wavy shape appeared; as the printing speed continued to increase, the curvature radius of the wavy shape became larger, and the waves tended to disappear; when the printing speed was 3 mm s^{-1}, uniform linear structures were printed; as the printing speed gradually exceeds the extrusion speed, the PZT jet did not break, but a "tail" was formed behind the printing nozzle, which was because the PZT slurry was a viscoelastic fluid with certain stretchability, and this property helped to obtain PZT structures with even smaller linewidths. The printing results under different printing heights and speeds were presented in Figure 3b. When the printing speed was relatively low, as the printing height increases, the curvature radius of the printed circles. This was because the excess linear parts undergo bending deformation and were subjected to greater gravitational force; when the printing speed was high and the printing height was low, the angle between the needle direction and the PZT jet became smaller, causing the needle to exert a greater shear force on the root of the linear slurry. And the PZT jet was prone to being pulled apart. However, when the height was too high, it indirectly increased the extension rate of the jet, which also led to the occurrence of broken lines.

The printed 3D PZT structure under various printing conditions was displayed in figure 3c. When the printing height of 3 mm, different printing speeds had an impact on the 3D PZT structure. Both the low speed and the high speed was not conducive to the successful printing of a well 3D PZT structure. When the printing speed was 2.5 mm s^{-1}, the line diameter of the square support structure was approximately 80 μm, and the line spacing was approximately 200 μm. This indicated that the printing method in this paper could be used to fabricate various 3D PZT structures. The SEM morphology images of the PZT 3D structure at different annealing temperatures was shown in figure 3d. As can be seen from the figures, after low-temperature annealing, the PZT 3D structure had small and incomplete grains, and there were many pores between the grains; after annealing at 1100 °C, the grains developed well, and the number of pores between the grains decreased. The SEM morphology image of the PZT 3D structure at 1100 °C annealing temperature (figure 3e). After 2 hours of annealing and holding treatment, the PZT 3D structure had fully developed grains, and the number of pores between the grains had significantly decreased. The results showed that the annealing temperature of 1100 °C and the holding time of 2 hours were relatively suitable annealing process parameters. Figure 3f shows the XRD patterns annealed at different temperatures. As can be seen from the figure, after annealing at 1100 °C for 2 hours, the diffraction peak at the (110) crystal plane of the PZT 3D structure was the highest, and there erre strong diffraction peaks at the (100), (111), (200), and (211) crystal planes, with no shift in the peak position and no garnet phase and other impurity phases were generated. Dielectric property tests of the 3D PZT structure (figure 3g) showed that both its relative permittivity and dielectric loss decreased with increasing frequency, measuring 1288 and 0.203 at 1 kHz, and decreasing to 1166 and 0.11 at 100 kHz, respectively, indicating good frequency stability.

3.2 Wavelet decomposition and reconstruction of strain signals

To effectively extract strain features during EMS trolley operation and suppress environmental noise, wavelet packet transform was employed for multi-scale analysis of the acquired signals. The low-frequency components (cA1-cA2) obtained from the decomposition of background signals exhibited smooth and continuous characteristics with small fluctuation amplitudes, reflecting the stable foundational part of the signal (Figure 4a). In contrast, the high-frequency components (cD1-cD3) showed significant fluctuations and abrupt changes, revealing rapidly varying information and interference components within the signal (figure 4b). After three levels of decomposition, the fluctuating characteristics of the cD1 component were particularly prominent, clearly representing high-frequency noise signals caused by external environmental interference.

Further signal characterization was achieved through wavelet packet tree decomposition (figure 4c). The signal curve corresponding to node (2,2) displayed pronounced fluctuation characteristics, consistent with the

https://doi.org/10.64486/m.65.3.8

behavior of the high-frequency signal cD1. This feature signal effectively captured the noise details in the background signal, providing data support for subsequent fault identification and signal purification, and facilitating the extraction of valid strain signals and noise removal in later processing stages. Time-frequency analysis of the background signal when the logistics vehicle was not passing over the track (figure 5a) revealed obvious energy fluctuations in the high-frequency region (>1 Hz), with frequency peaks showing multiple significant variations, indicating the presence of notable environmental noise or interference signals during this period. After wavelet denoising processing (figure 5b-c), the reconstructed signal exhibited significantly stationary characteristics with markedly reduced amplitude fluctuations. The time-frequency analysis indicated that the noise signal frequency was primarily concentrated above 1 Hz with an energy amplitude less than 25. After denoising and reconstruction, the amplitude of internal wave peaks was mainly concentrated between 20 and 40. Identifying the frequency and amplitude characteristics of the noise signal allows for further reduction of its interference with feature extraction, thereby improving signal analysis accuracy.

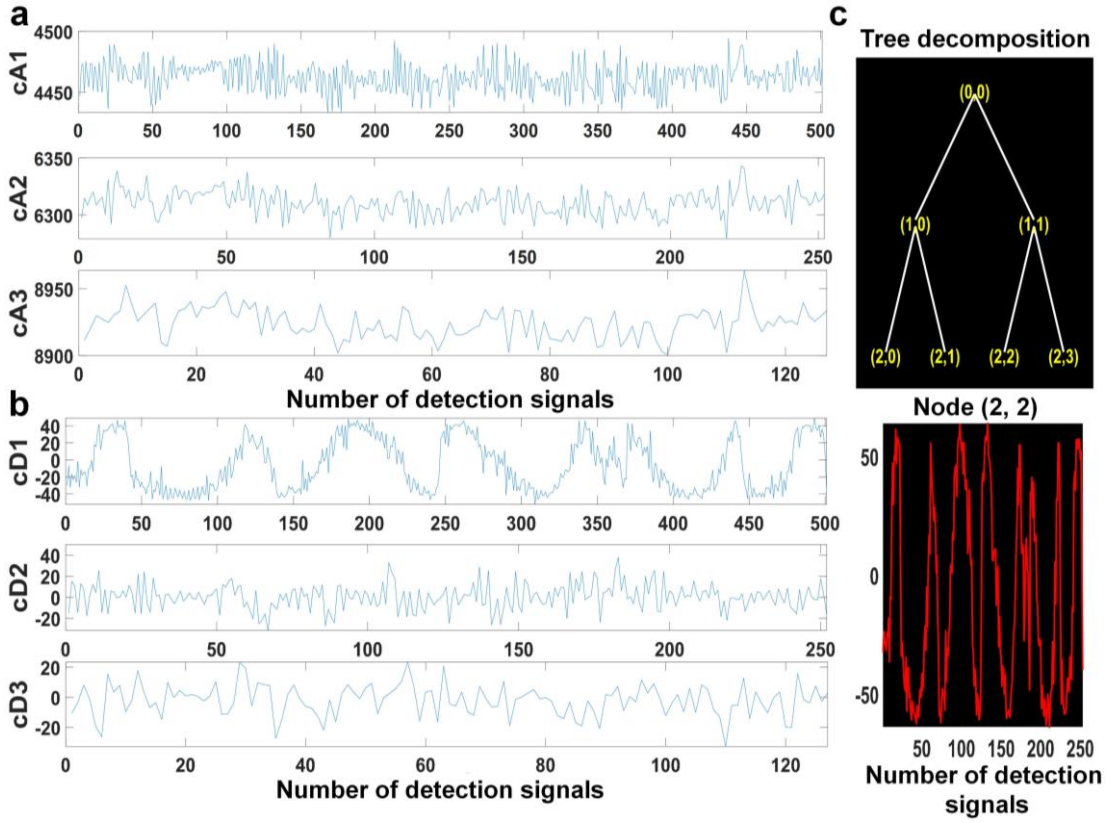

Figure 4. Wavelet decomposition of background signal. (a) Low-frequency signal waveform, (b) High-frequency signal waveform, (c) Tree decomposition graph, and (2, 2) node signal.

Comparing the decomposition results of strain signals under no-load and full-load conditions (figure 6), it was found that cA1-cA3 primarily contained low-frequency components, representing the relatively stable structural information in the original signal, while cD1-cD3 mainly contained high-frequency components, manifesting as irregular and rapid fluctuations. After three-level wavelet decomposition, the low-frequency signals showed high similarity to the original signal. In particular, the cA1 signal was almost identical in waveform and characteristics to the node (2,0) signal in the wavelet packet decomposition (figure 4), indicating that this part retained the main effective information of the signal. In contrast, the high-frequency signals were more disordered and could be removed as noise components in subsequent analyses to enhance signal quality.

Notably, significant differences were observed in the decomposition results of strain signals between no-load and full-load conditions. Under full load, the peak part of the signal waveform exhibited two distinctly different gradient changes during the descent stage. This difference suggests that as the logistics vehicle passes

https://doi.org/10.64486/m.65.3.8

the monitoring point, the material box transporting tobacco and the EMS logistics vehicle itself exert strain effects of varying degrees on the track, jointly contributing to the signal superposition process.

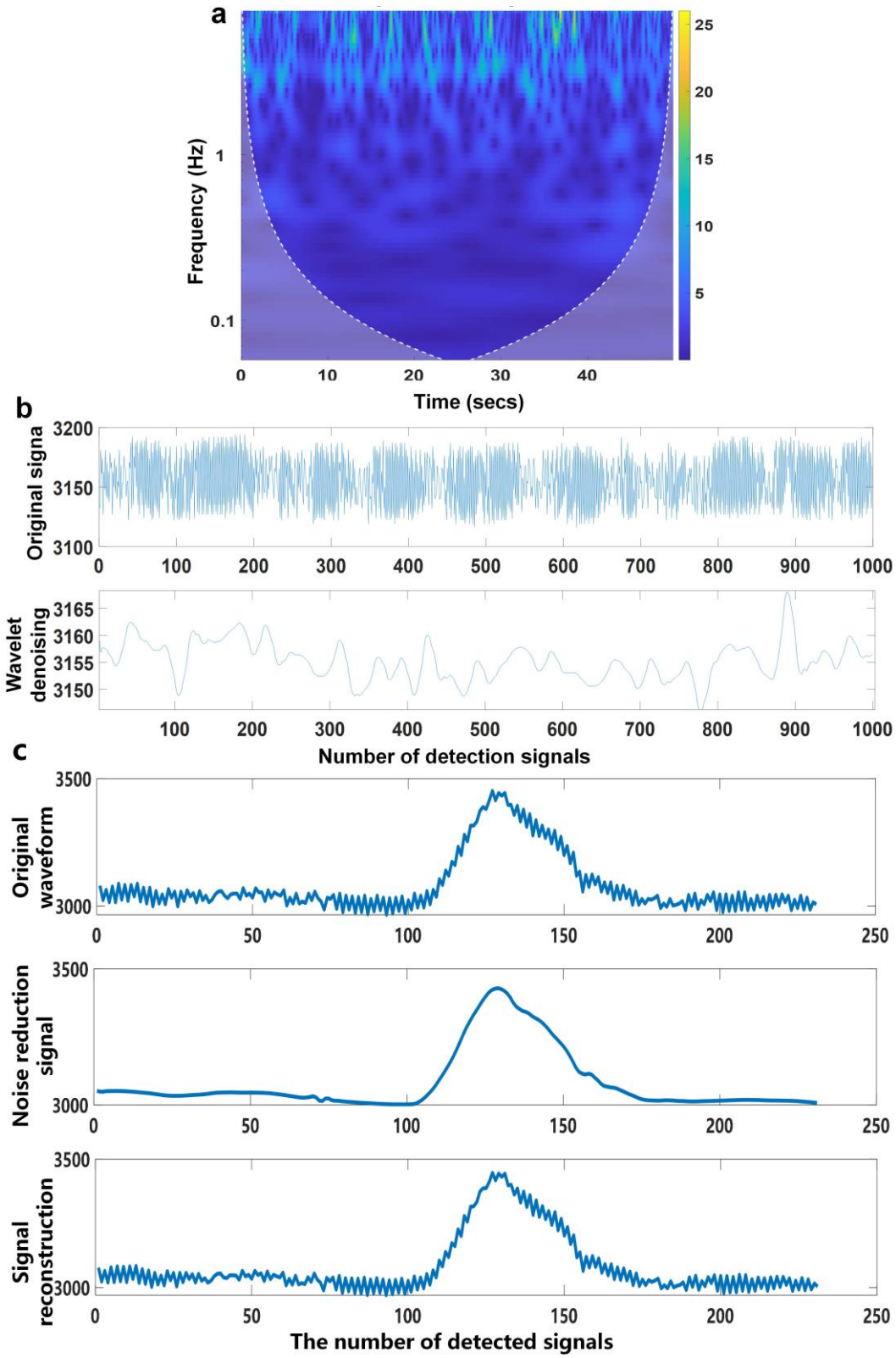

Figure 5. Time-frequency analysis and noise reduction reconstruction of background signal. (a) Time-frequency analysis diagram, (b-c) Noise reduction process of background signal.

https://doi.org/10.64486/m.65.3.8

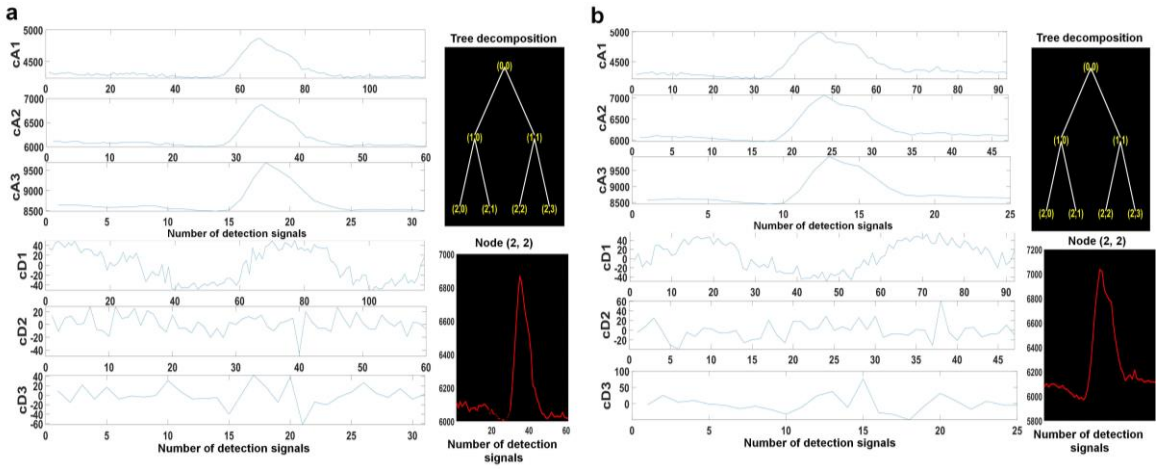

Figure 6. Wavelet decomposition of strain signals in different states of the orbit. (a) Signal decomposition results under no-load state, (b) Strain signals under full-load state.

Based on the operational state of the EMS logistics vehicle, signals were analyzed separately for no-load and full-load conditions. The time-frequency analysis results obtained via wavelet transform (figure 7a-b) showed that signals from both states shared similar low-frequency characteristics. However, the energy of the high-frequency components was more significant under full-load conditions, especially in the frequency range above 1 Hz, where the energy peaks were higher than those in the no-load state. This indicates that the logistics vehicle has a greater impact on the track strain signal when carrying goods.

The strain signal in the no-load state, after wavelet decomposition and reconstruction, exhibited a smoother waveform. Following noise removal, the signal fluctuation was significantly weakened and the amplitude markedly reduced, suggesting a relatively smaller noise component. In contrast, the processed full-load state strain signal still exhibited certain high-frequency fluctuations in the peak region, indicating that due to the influence of the material box, some high-frequency noise is still generated during the loading process, although the overall noise level was significantly reduced after denoising. Pearson correlation coefficient analysis was conducted to examine the linear relationships among feature parameters (figure 7c). High correlations were found among features such as rms, root, and mean, indicating they share similar numerical trends. To avoid multicollinearity issues, it is necessary to eliminate some of these redundant features. In comparison, the correlation coefficients between mean and other features were relatively small, suggesting this feature is less associated with other variables. Therefore, removing the mean feature was considered to enhance model robustness.

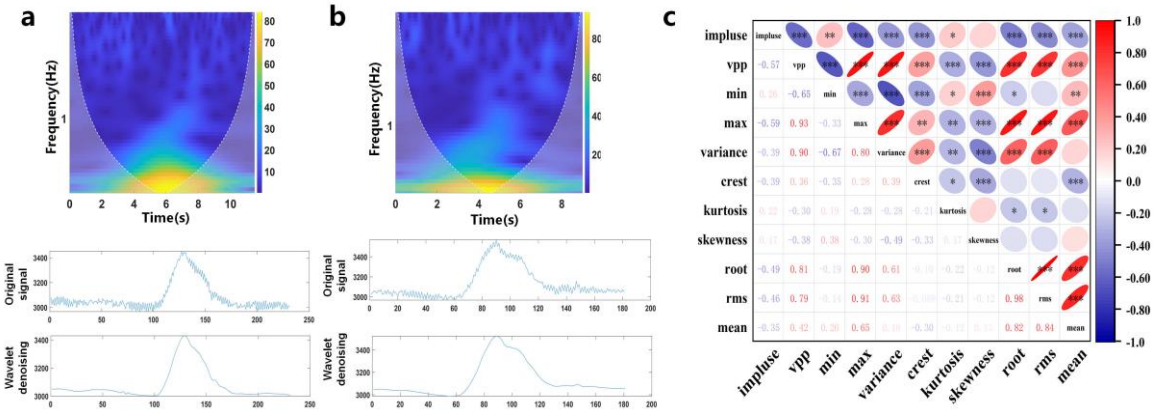

Figure 7. Time-frequency analysis and noise reduction reconstruction. (a) Time-frequency analysis diagram of no-load signal and noise reduction process of no-load signal, (b) Time-frequency analysis diagram of full load signal and noise reduction process of full load signal, (c) Correlation coefficient matrix of characteristic parameters.

https://doi.org/10.64486/m.65.3.8

3.3 Shapley Analysis

To evaluate the contribution of different features to model prediction, Shapley value analysis was employed for quantitative assessment. The feature contribution bar chart (figure 8a) revealed that features such as max, rms, and crest contributed significantly to the model, indicating their important role in prediction. In contrast, features like kurtosis and impulse showed relatively lower contribution degrees, suggesting they have a smaller impact on model prediction for this specific task.

The Shapley value distribution scatter plot further elucidated the influence patterns of each feature (figure 8b). Features like max and rms generally exerted a strong positive or negative influence on the model output in most cases, whereas the influence of features like impulse and kurtosis was relatively weak and insignificant. The four features—max, rms, crest, and variance—demonstrated consistent behavior in both the Shapley plot and the contribution plot, all contributing highly to model prediction. This suggests that prioritizing these features during model optimization can improve model accuracy.

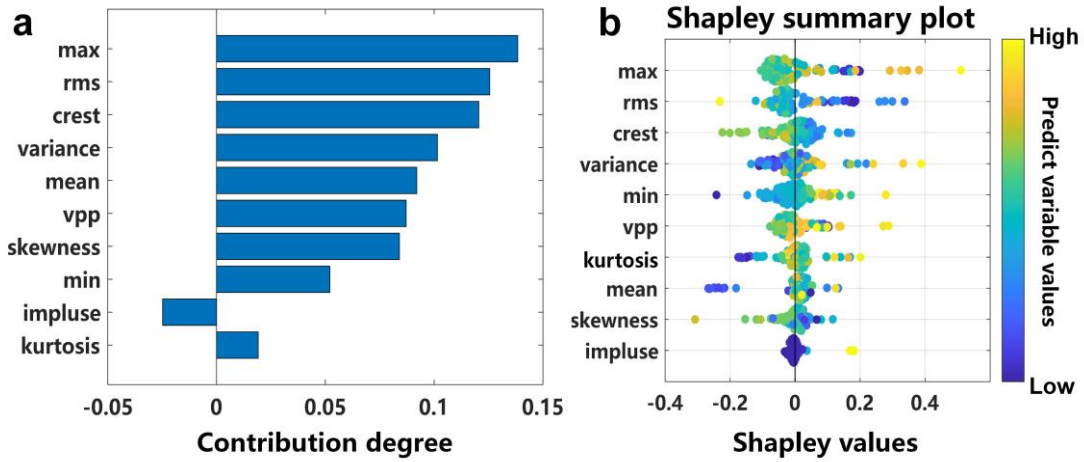

Figure 8. Analysis of the contribution degree of different features to model prediction. (a) Histogram of the contribution degree of features to the model, (b) Distribution of Shapley values for each feature.

3.4 Comparison of machine learning models

In this study, fault signals were categorized into five classes: no-load state (Label 1), full-load state (Label 2), no-load loading state (Label 3), full-load no-box state (Label 4), and abnormal state (Label 5). These labels distinguish the states of EMS logistics vehicles at different operational stages. By rationally setting these classification labels and employing a Bayesian optimization method, model hyperparameters can be effectively optimized to improve classification accuracy. Figure 9 presents the hyperparameter optimization curves for six machine learning models: Convolutional Neural Network (CNN), Kernel method (Kernel), K-Nearest Neighbors (KNN), Support Vector Machine (SVM), Naive Bayes, and Discriminant Analysis, with a maximum iteration number set to 30. As the iteration number increased, the minimum classification error for each model gradually decreased until the gradient flattened or vanished. After exceeding 15 iterations, the classification error stabilized, with the minimum error for most models dropping below 0.3.

It is noteworthy that for some models (Figure 9b, d, e), the optimal hyperparameter point did not coincide with the minimum error hyperparameter point, indicating potential overfitting, where the model fails to achieve the global minimum error under certain hyperparameter combinations. For other models, the coincidence of these points signifies optimal performance under that specific hyperparameter set. Although the KNN model achieved a relatively low minimum classification error, its requirement for a high number of iterations resulted in longer training times, which may impact practical application. In comparison, the Discriminant Analysis model required fewer iterations but exhibited a significantly higher minimum classification error than other models, indicating relatively poorer classification performance. Considering both classification error and

https://doi.org/10.64486/m.65.3.8

training efficiency, the neural network model demonstrates superior potential and can serve as a foundation for further optimization in classification tasks.

Figure 9 (g-l) shows the Receiver Operating Characteristic (ROC) curves for each model, used to evaluate binary classification performance. A curve closer to the top-left corner indicates better model performance, maximizing the true positive rate while minimizing the false positive rate. The Area Under the Curve (AUC) quantitatively assesses overall model performance, with a value closer to 1 indicating stronger classification capability. For the five different classification labels, the AUC values and corresponding ROC curves varied among models. Overall, most ROC curves were above the diagonal (random classification line), while a few fell below it, indicating poor performance for some models on specific labels. Particularly for Label 5, some ROC curves from different models fell below the diagonal, suggesting that the neural network is relatively more sensitive in handling this label. For other labels, models with higher AUC values demonstrated superior classification capabilities: SVM was best for Label 4, neural network for Label 3, KNN for Label 2, and a combination of Kernel Approximation, KNN, and Naive Bayes dominated for Label 1. Variance analysis of the AUC values across different models, after removing those with AUC below 0.7, revealed that the neural network had a higher variance, indicating greater performance variability across different labels.

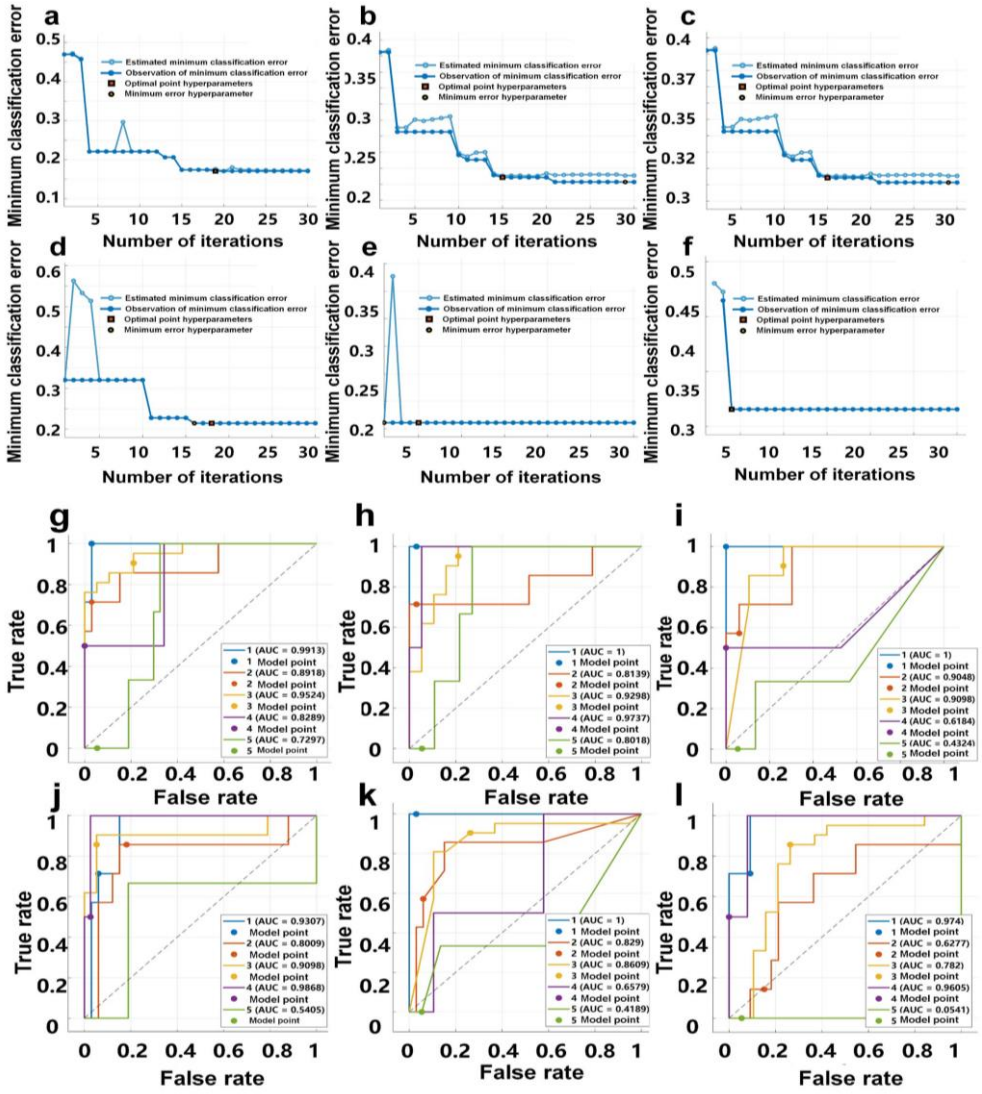

Figure 9. (a-f) Hyperparameter optimization curve, (a, CNN; b, Kernel; c, KNN; d, SVM; e, Naive Bayes; f, discriminant), (g-l) Receiver operating characteristic curve (ROC) of each model, (g, CNN; h, Kernel; i, KNN; j, SVM; k, Naive Bayes; l, discriminant).

https://doi.org/10.64486/m.65.3.8

4. Conclusions

This study proposes a novel fault diagnosis scheme for EMS trolley systems, which combines 3D printed customized PZT sensors with machine learning. This method first uses a dedicated sensor prepared by printing to collect strain signals. The effects of annealing temperature and annealing time on the crystal phase and microstructure of PZT thick films and 3D structures were investigated. It determined the more suitable annealing process parameters, and characterizes the piezoelectric properties, dielectric properties of PZT thick films, and the impedance characteristics of piezoelectric microcantilever beams. Secondly, the neural network fusion Bayesian hyperparameter optimization technique was adopted to systematically optimize the network topology structure in order to obtain the optimal network weights and thresholds. Experimental verification shows that the accuracy rate of the neural network model optimized by this method in fault detection reaches 91.07 %. The predictive capabilities of various models were compared and analyzed, and the accurate diagnosis of EMS electric vehicle system faults was achieved. This system can accurately determine the operating status of EMS trolleys, providing effective theoretical support and practical technical solutions for their fault detection and daily operation and maintenance work.

Acknowledgments: This project was supported by the National Natural Science Foundation of China (52575403), China Postdoctoral Science Foundation (2024M753510), Natural Science Foundation of Zhejiang Province (LMS26E050021), Ningbo Natural Science Foundation (2024J427, 2023J376, 2022J008), Ningbo Yongjiang Talent Introduction Programme (2021A-137-G), and Ningbo Zhenhai 14th Five-Year Plan's Technological Breakthrough Projects (2022001).

References

[1] M. A. Uddin, M. Debnath, S. Roy, S. Adiba, and M. M. A. Talukder, "Identifying the smoking and smokeless tobacco-related predictors on frequencies of heavy vehicle traffic accidents in Bangladesh: Linear and binary logistic regression-based approach," *Advances in Civil Engineering*, vol. 2023, Art. no. 7116057, 2023, https://doi.org/10.1155/2023/7116057

[2] V. Cirillo, F. S. Massimo, M. Rinaldini, J. Staccioli, and M. E. Virgillito, "Monopoly power upon the world of work: A workplace analysis in the logistics segment under automation," *Review of Political Economy*, 2024, https://doi.org/10.1080/09538259.2024.2419611

[3] X. Wang, Q. Gao, D. W. Schubert, and X. Liu, "Review on electrospun conductive polymer composites strain sensors," *Advanced Materials Technologies*, vol. 8, no. 16, Art. no. 2300293, 2023, https://doi.org/10.1002/admt.202300293

[4] Y. Cheng and J. Yu, "Performance investigation on strain sensors with wavy structures for direction perception," *Sensors and Actuators A: Physical*, vol. 383, Art. no. 116194, 2025, https://doi.org/10.1016/j.sna.2024.116194

[5] J. Shi *et al.*, "Crack control in biotemplated gold films for wide-range, highly sensitive strain sensing," *Advanced Materials Interfaces*, vol. 6, no. 20, Art. no. 1901223, 2019, https://doi.org/10.1002/admi.201901223

[6] J. H. Lee *et al.*, "Heterogeneous structure omnidirectional strain sensor arrays with cognitively learned neural networks," *Advanced Materials*, vol. 35, no. 13, Art. no. 2208184, 2023, https://doi.org/10.1002/adma.202208184

[7] M. Regehly *et al.*, "Xolography for linear volumetric 3D printing," *Nature*, vol. 588, no. 7839, pp. 620–624, 2020, https://doi.org/10.1038/s41586-020-3029-7

[8] S. Zhao *et al.*, "Additive manufacturing of silica aerogels," *Nature*, vol. 584, no. 7821, pp. 387–392, 2020, https://doi.org/10.1038/s41586-020-2594-0

[9] W. Jung *et al.*, "Three-dimensional nanoprinting via charged aerosol jets," *Nature*, vol. 592, no. 7852, pp. 54–59, 2021, https://doi.org/10.1038/s41586-021-03353-1

[10] J. Zhang *et al.*, "Ultrauniform, strong, and ductile 3D-printed titanium alloy through bifunctional alloy design," *Science*, vol. 383, no. 6683, pp. 639–645, 2024, https://doi.org/10.1126/science.adj0141

[11] C. Zhao *et al.*, "Critical instability at moving keyhole tip generates porosity in laser melting," *Science*, vol. 370, no. 6520, pp. 1080–1084, 2020, https://doi.org/10.1126/science.abd1587

[12] T. Polonsky and T. M. Pollock, "Closing the science gap in 3D metal printing," *Science*, vol. 368, no. 6491, pp. 583–584, 2020, https://doi.org/10.1126/science.abb4938

https://doi.org/10.64486/m.65.3.8

[13] D. Wang *et al.*, "Large-area polymer semiconductor sub-microwire arrays by coaxial focused electrohydrodynamic jet printing for high-performance OFETs," *Nature Communications*, vol. 13, Art. no. 6214, 2022, https://doi.org/10.1038/s41467-022-34015-z

[14] Q. Wang *et al.*, "High-resolution, flexible, and full-color perovskite image photodetector via electrohydrodynamic printing of ionic-liquid-based ink," *Advanced Functional Materials*, vol. 31, no. 28, Art. no. 2100857, 2021, https://doi.org/10.1002/adfm.202100857

[15] M. S. Onses *et al.*, "Mechanisms, capabilities, and applications of high-resolution electrohydrodynamic jet printing," *Small*, vol. 11, no. 34, pp. 4237–4266, 2015, https://doi.org/10.1002/smll.201500593

[16] K. Li *et al.*, "Printed bioinspired piezoelectric nano-hair for ultrahigh sensitive airflow detection," *Chemical Engineering Journal*, vol. 490, 2024. https://doi.org/10.1016/j.cej.2024.151570

[17] K. Li *et al.*, "3D printed ultrahigh aspect ratio lead zirconate titanate (PZT) nanostructures for nano-newton force sensing," *Journal of the European Ceramic Society*, vol. 44, no. 7, pp. 4646–4656, 2024, https://doi.org/10.1016/j.jeurceram-soc.2024.02.003

[18] O. Tropsha, O. Isayev, A. Varnek, G. Schneider, and A. Cherkasov, "Integrating QSAR modelling and deep learning in drug discovery: The emergence of deep QSAR," *Nature Reviews Drug Discovery*, vol. 23, no. 2, pp. 141–155, 2024, https://doi.org/10.1038/s41573-023-00832-0

[19] Y. Zhang *et al.*, "Deep long-tailed learning: A survey," *IEEE Transactions on Pattern Analysis and Machine Intelligence*, vol. 45, no. 9, pp. 10795–10816, 2023, doi: https://doi.org/10.1109/TPAMI.2023.3268118.

[20] X. Yang *et al.*, "A survey on deep semi-supervised learning," *IEEE Transactions on Knowledge and Data Engineering*, vol. 35, no. 9, pp. 8934–8954, 2023, https://doi.org/10.1109/TKDE.2022.3220219

[21] J. X. Li *et al.*, "An improved lightweight network architecture for identifying tobacco leaf maturity based on deep learning," *Journal of Intelligent & Fuzzy Systems*, vol. 41, no. 2, pp. 4149–4158, 2021, https://doi.org/10.3233/JIFS-210640

[22] N. Vu Viet *et al.*, "Hybrid machine learning approaches for landslide susceptibility modeling," *Forests*, vol. 10, no. 2, Art. no. 157, 2019, https://doi.org/10.3390/f10020157

[23] A. Shafiq *et al.*, "Reliability modeling and analysis of mixture of exponential distributions using artificial neural network," *Mathematical Methods in the Applied Sciences*, vol. 47, no. 5, pp. 3308–3328, 2024, https://doi.org/10.1002/mma.8178

[24] J. Duan *et al.*, "Short-term wind power forecasting using the hybrid model of improved variational mode decomposition and correntropy long short-term memory neural network," *Energy*, vol. 214, Art. no. 118980, 2021, https://doi.org/10.1016/j.energy.2020.118980

[25] Q. Fan, Z. Zhang, and X. Huang, "Parameter conjugate gradient with secant equation-based Elman neural network and its convergence analysis," *Advanced Theory and Simulations*, vol. 5, no. 9, Art. no. 2200047, 2022, https://doi.org/10.1002/adts.202200047

[26] J. Berg and K. Nystrom, "A unified deep artificial neural network approach to partial differential equations in complex geometries," *Neurocomputing*, vol. 317, pp. 28–41, 2018, https://doi.org/10.1016/j.neucom.2018.06.056

[27] S. Wang, X. Yu, and P. Perdikaris, "When and why PINNs fail to train: A neural tangent kernel perspective," *Journal of Computational Physics*, vol. 449, Art. no. 110768, 2022, doi: https://doi.org/10.1016/j.jcp.2021.110768.

[28] B. Bischl *et al.*, "Hyperparameter optimization: Foundations, algorithms, best practices, and open challenges," *WIREs Data Mining and Knowledge Discovery*, vol. 13, no. 2, Art. no. e1484, 2023, doi: https://doi.org/10.1002/widm.1484.

[29] Y. Ali *et al.*, "Hyperparameter search for machine learning algorithms for optimizing the computational complexity," *Processes*, vol. 11, no. 2, Art. no. 21, 2023, https://doi.org/10.3390/pr11020349

[30] H. Victoria and G. Maragatham, "Automatic tuning of hyperparameters using Bayesian optimization," *Evolving Systems*, vol. 12, no. 1, pp. 217–223, 2021, doi: https://doi.org/10.1007/s12530-020-09345-2.

[31] V. Kulshrestha, V. Krishnaswamy, and M. Sharma, "Bayesian BiLSTM approach for tourism demand forecasting," *Annals of Tourism Research*, vol. 83, Art. no. 102925, 2020, https://doi.org/10.1016/j.annals.2020.102925

[32] X.-B. Jin *et al.*, "Deep spatio-temporal graph network with self-optimization for air quality prediction," *Entropy*, vol. 25, no. 2, Art. no. 247, 2023, https://doi.org/10.3390/e25020247

[33] K. Zhang *et al.*, "Beyond a Gaussian denoiser: Residual learning of deep CNN for image denoising," *IEEE Transactions on Image Processing*, vol. 26, no. 7, pp. 3142–3155, 2017, https://doi.org/10.1109/TIP.2017.2662206

[34] Z. Huang *et al.*, "A general Gaussian heatmap label assignment for arbitrary-oriented object detection," *IEEE Transactions on Image Processing*, vol. 31, pp. 1895–1910, 2022, https://doi.org/10.1109/TIP.2022.3148874

[35] X. Fu *et al.*, "Lightweight pyramid networks for image deraining," *IEEE Transactions on Neural Networks and Learning Systems*, vol. 31, no. 6, pp. 1794–1807, 2020, https://doi.org/10.1109/TNNLS.2019.2926481

https://doi.org/10.64486/m.65.3.8